Journal of Electrochemistry

Volume 22
Issue 2 *Special issue of Electrocatalyst and Electrocatalysis in Fuel Cells(Editor: Professor WEI Zi-dong)*

2016-04-28

Multi-Scaled Carbon Supported Platinum as a Stable Electrocatalyst for Oxygen Reduction Reaction

Yu-ping LI

Lu-hua JIANG
Dalian National Laboratory for Clean Energy, Dalian Institute of Chemical Physics, Chinese Academy of Sciences, Dalian 116023, China;, sunshine@dicp.ac.cn

Su-li WANG

Gong-quan SUN
Dalian National Laboratory for Clean Energy, Dalian Institute of Chemical Physics, Chinese Academy of Sciences, Dalian 116023, China;, gqsun@dicp.ac.cn

Recommended Citation

Yu-ping LI, Lu-hua JIANG, Su-li WANG, Gong-quan SUN. Multi-Scaled Carbon Supported Platinum as a Stable Electrocatalyst for Oxygen Reduction Reaction[J]. *Journal of Electrochemistry*, 2016 , 22(2): 135-146.
DOI: 10.13208/j.electrochem.151149
Available at: https://jelectrochem.xmu.edu.cn/journal/vol22/iss2/6

DOI: 10.13208/j.electrochem.151149 **Artical ID**:1006-3471(2016)02-0135-12
Cite this: *J. Electrochem.* **2016**, *22*(2): 135-146 **Http**://electrochem.xmu.edu.cn

Multi-Scaled Carbon Supported Platinum as a Stable Electrocatalyst for Oxygen Reduction Reaction

LI Yu-ping[1,2], JIANG Lu-hua[1*], WANG Su-li[1], SUN Gong-quan[1*]
(1. *Dalian National Laboratory for Clean Energy, Dalian Institute of Chemical Physics, Chinese Academy of Sciences, Dalian* 116023, *China*; 2. *University of Chinese Academy of Sciences, Beijing* 100039, *China*)

Abstract: The stability of carbon supports is essential for electrocatalysts of fuel cells. Herein, the mesoporous carbon with the high graphitic degree (highly graphitic mesoporous carbon, HGMC) was synthesized by using resorcinol as the carbon precursor, SiO_2 as the templates and urea as the reducing agent. The as-prepared HGMC was characterized by XRD, Raman spectroscopy, TEM, N_2 adsorption. The stability of HGMC was evaluated by mimicking the start-up/shut-down conditions of fuel cells in a three-electrode system referring to the NREL standard. The obtained HGMC is of moderate surface area (187.4 $m^2 \cdot g^{-1}$) and is chemically stable under potentiodynamic cycling as compared to the commercial Vulcan XC-72, while the high graphitic structure is adverse to the mass transport. To overcome the drawback of the HGMC in mass transportation, MWCNTs was introduced as a spacer to construct a 3D multi-scaled support. Compared to the single HGMC supported Pt catalyst and the commercial Pt/C-JM catalyst, the multi-scaled MSGC (the mixture of HGMC and MWCNTs with a mass ratio of 1:1) supported Pt catalyst displayed both enhanced electrochemical stability and significantly improved mass transportation for the oxygen reduction reaction, due to the stability and the multi-scaled structure of the carbon supports.

Key words: carbon support; platinum; oxygen reduction reaction; fuel cell
CLC Number: O646 **Document Code**: A

Carbon supports play a crucial role for electrocatalysts of fuel cells, in which on one side, it provides large surface area for metal particles to be dispersed uniformly, and on the other side, three dimensional (3D) carbon supports construct a highly porous electrode allowing reactants/products being transport conveniently. Historically, the highly-dispersed carbon supported platinum or platinum alloy as the alternative of the platinum black has been recognized as a milestone in the development of fuel cells [1-2]. Presently, Vulcan XC-72 produced by Cabot Corporation is the most widely used carbon support for fuel cell electrocatalysts considering the high surface area (around 250 $m^2 \cdot g^{-1}$) and the suitable pore distribution/particle size. However, due to the low graphitic degree, and thus, large amounts of defects and functional groups on surface, it is easy to be corroded. Especially under operating conditions, the cathodic potential could reach up to 1.6 V during the startup and shutdown of fuel cells[3], thereby, the carbon supports would suffer from severe electrochemical corrosion. The direct detrimental effect of the corrosion of carbon supports is the detachment of Pt nanoparticles from carbon and the subsequently aggregate. As a result, the fuel cell performance would decrease significantly[4-10]. Moreover, the micropores in carbon, although contribute significantly to surface area, is believed to be harmful to mass transportation and the

Received: 2016-01-04, Revised: 2016-04-15 *Corresponding author, Tel: (86-411)84379603, E-mail: sunshine@dicp.ac.cn, gqsun@dicp.ac.cn
This work is financially supported by the Strategic Priority Research Program of the Chinese Academy of Science (Grant No. XDA09030104), the National Basic Research Program of China (973 Program, Grant No. 2012CB215500) and the Key Program of the Chinese Academy of Science (Grant No. KGZD-EW-T08).

active components confined in micropores are unavailable to reactants. To construct stable carbon materials tailored to nanoparticle anchoring and gas/liquid mass transportation is highly necessary for fuel cells.

In the past decades, great efforts have been taken to improve the electrochemical stability of the-state-of-the-art carbon supports. Pre-treatment of the activated carbons at elevated temperatures could eliminate the functional groups at the carbon edges and re-organizing the carbon atoms in matrix, which has become a main approach to improve the graphitic degree of carbon materials and the corrosion resistance. However, in such a process, the surface area of carbon usually decreases tremendously, which is adverse to the dispersion of Pt nanoparticles. With the development of synthesis techniques, alternative corrosion-resistant carbons, e.g., carbon nanotubes (CNTs)[11-19], nanofibers (CNFs), nanohorns (CNHs)[20-21], and graphene[22], were synthesized. These novel carbon materials have both high graphitic degree and large surface area, which are potential supports for metal nanoparticles. To load more metal nanoparticles uniformly, these perfect carbon matrix composed of hexatomic rings have to be modified with functional groups; moreover, the laminar structured carbon, such as graphene, tends to overlap and thus adverse to mass transportation of reactants/products[23-24]. To obtain both active and stable electrocatalysts, a balance among graphitic degree, functional groups and surface area of carbon supports is required.

In our previous work[25], we reported a graphitic mesoporous carbon (GMC) with a surface area of 403 $m^2 \cdot g^{-1}$ acting as the support for PtRu naoparticles to catalyze methanol electro-oxidation. Although the electrochemical stability of the GMC was satisfied benefiting from the high graphitic degree, it was facing poor mass transportation due to its tendency of stacking. In this article, aiming at constructing both stable and mass transport facilitated carbon materials, one side, we synthesized a highly graphitic mesoporous carbon (HGMC) with surface area of 187.4 $m^2 \cdot g^{-1}$ by adopting a modified thermal treatment approach[25] to increase graphitic degree ever further and the other side, to overcome the drawback of the HGMC in mass transportation, multi-wall carbon nanotubes (MWCNTs) were used as spacers to be physically mixed with the HGMC to construct 3D multi-scaled carbon supports for Pt nanoparticles. The obtained multi-scaled carbon supported Pt was used as the electrocatalyst for oxygen reduction reaction (ORR), and the electrochemical tests suggest that it displayed better activity and stability than the Vulcan XC-72 supported Pt, which are ascribed to the smaller sized Pt particles, the facilitated mass transportation of reactants/products and the good electrochemical stability of the multi-scaled carbon supports.

1 Experimental Section

1.1 Preparation of GMC and HGMC

The preparation of GMC is referred to our previous work[25]. To prepare HGMC, the procedure is modified. In detail, 6.464 g $Fe(NO_3)_3 \cdot 9H_2O$ and 4.706 g sodium citrate were dissolved in 10 mL deionized water, then 3.840 g SiO_2-sol (NYACOL1440, IKA) and 4.404 g resorcinol were added into the solution by turns. Different from the procedure to prepare the GMC, 2.400 g urea was additionally introduced to the above mixture and stirred for 10 min. Then, 6.4 mL formaldehyde solution (37%, by mass) was poured into the mixture under vigorous stirring until the mixture turned into dark red gel (named RF). The RF gel was cured for 3 hours at 85 °C in water bath and dried to get RF powder containing iron salt. The RF powder was heated in nitrogen atmosphere at 900 °C for 3 h. The obtained composite was then refluxed in 3 $mol \cdot L^{-1}$ NaOH solution and 5 $mol \cdot L^{-1}$ HNO_3 solution, respectively, to remove silica and iron. Finally, the powder was washed and dried to obtain HGMC.

1.2 Preparation of Electrocatalysts

The preparation of electrocatalyst was referred to a modified ploy ol process developed in our lab[26]. Briefly, certain amount of $H_2PtCl_6 \cdot 6H_2O$ was diluted into ethylene glycol and the pH value of the solution was adjusted up to 13 with sodium hydroxide. After being stirred for 15 min, the mixture was then heated

to 130 °C and maintained for 3 h to get deep-brown Pt colloid. After cooled down to 80 °C, a fixed amount of HGMC was dispersed into ethylene glycol and was added to the Pt colloid, and then pH value was adjusted to 2 with hydrochloric acid. After continuously stirred for 2 h, the slurry was filtered and the filtrate was analyzed by the XRF to make sure that Pt was completely loaded on the supports. After washed with deionized water, the black filter cake was dried in a vacuum oven under 75 °C overnight. Finally, the carbon supported Pt was obtained and denoted as Pt/HGMC. Alternatively, the mixture of HGMC and MWCNTs with a mass ratio of 1:1 was added to the Pt colloid as the support to obtain Pt/MSGC.

1.3 Physical Characterization

X-ray diffraction (XRD) patterns were recorded on Philips X'pert Pro X-ray diffractometer equipped with a Cu K_α1 (λ = 1.54 Å) radiation at 40 kV and 40 mA. The scan rate was 10°·min^{-1} with angular resolution of 0.02°. The Raman spectroscopy was conducted on Jobin Yvon Lab RAM HR800 triple stage spectrograph. He-Ne laser was used as an excitation source with an output power of 1 mW. The laser line was 532 nm and the signal was collected by CCD. The Brunauer-Emmett-Teller (BET) surface area and the pore size distribution of the samples were obtained from N_2 adsorption isotherms at 77 K (Nova 2200e, Quantachrome). Before adsorption analysis, samples were degassed under 300 °C for 6 h in vacuum. The equilibrium time and equilibrium timeout are 200 s and 400 s, respectively. Transmission electron microscope (TEM) images were obtained by JEOL JEM-2000EX operated under 120 kV. The XRF analysis was conducted on ARL QUANT'X EDXRF Analyser (Thermo Scientific) under Mid Zb mode.

1.4 Electrochemical Characterization

Electrochemical measurements were conducted on a CHI 760B, using a typical three-electrode cell with a Pt wire as a counter electrode and a saturated calomel electrode (SCE, 0.302 V vs. RHE in 0.1 mol·L^{-1} $HClO_4$) as a reference electrode. A salt bridge was used to prevent contamination of Cl^- to electrolyte and the catalyst. The working electrode was prepared via the procedure described in literature[27-29]. Briefly, graphitic carbon or catalyst was typically dispersed in a water/Nafion-inomer/ethanol (volume ratio of water, 5% by mass, Nafion-inomer solution and ethanol was 1:1:100) solution to form uniform ink of 5 mg·mL^{-1} and 2.5 mg·mL^{-1}, respectively. Glassy carbon rotating disc electrode (5 mm in diameter) was polished and cleaned to mirror firstly, then 20 μL of the ink was pipetted on the glassy carbon area and dried to form a thin uniform catalyst film. The Pt loading on the glassy carbon is 100 μg.cm^{-2}.

Prior to determination of the electrochemical active surface areas and the ORR activity, the work electrode was electrochemically cleaned in N_2 saturated 0.1 mol·L^{-1} $HClO_4$ by potentially cycling from 0.05 to 1.4 V vs. RHE with a scan rate of 100 mV·s^{-1}. Cyclic voltammetry curves were recorded in N_2 saturated 0.1 mol·L^{-1} $HClO_4$ and the potential is between 0.05 to 1.3 V versus RHE with sweep rate of 10 mV·s^{-1}. The ORR polarization curves were obtained under the same scan range along with scan rate but in O_2-saturated 0.1 mol·L^{-1} $HClO_4$ at rotating rate of 1600 r·min^{-1}. The accelerating aging tests mimicking the conditions during the start-up/shut-down of fuel cells was conducted in the sweeping range of 1.0 to 1.6 V (versus RHE) and the scanning rate of 100 mV·s^{-1} in N_2 purged 0.1 mol·L^{-1} $HClO_4$. The carbon black (Vulcan XC-72, Cabot) and carbon black supported Pt (Pt/C, Johnson Matthey, HispecTM4000) are used as the control groups. The Vulcan XC-72 was refluxed at 130 °C in 5 mol·L^{-1} HNO_3 solution to remove ash and other impurities before characterization.

2 Results and Discussion

The XRD patterns of the HGMC, GMC and Vulcan XC-72 are presented in Fig. 1A. The diffraction peaks in the patterns located at 26.4°, 42.8°, 54°, 78° can be assigned to (002), (100)/(101), (004) and (110) of graphite, respectively (JCPDS:PDF75-1621). Both HGMC and GMC have sharper diffraction peaks than Vulcan XC-72, indicating a higher graphitic degree due to the function of graphitic cata-

lyst, metallic iron or iron carbonate[30-32]. Furthermore, compared with GMC, HGMC displays even sharper diffraction peaks, indicating the graphitic structure in HGMC is more well-defined. This may be attributed to the function of urea, which is regarded as an effective reducing agent in removing oxygen-containing groups intercalated into the interlayer spacing of graphite[33]. Meanwhile, the lattice distance between two neighbored graphite (002) facets, calculated from the Bragg's equation, is 0.34 nm for both HGMC and GMC, as listed in Tab. 1, closer to that of ideal graphite, 0.34 nm[34], while the lattice distance for Vulcan XC-72 is 0.36 nm, suggesting that HGMC and GMC possess higher graphitic degree than Vulcan XC-72. Further evidence is provided by the Raman spectra of HGMC, GMC and Vulcan XC-72 in Fig 1B. The Raman spectra are fitted to four Lorentzian peaks, located at 1200 cm^{-1}, 1350 cm^{-1}, 1510 cm^{-1}, and 1590 cm^{-1}, respectively. The resonance peak at 1590 cm^{-1} (always denoted as G band) is ascribed to the planar motion of sp^2-hybridized carbon atoms while the one located at 1350 cm^{-1} (usually denoted as D band) corresponds to the defects in graphene structure[35-36]. Meanwhile, the peaks locate at 1200 cm^{-1} and 1510 cm^{-1} are attributed to those carbon atoms outside of planar graphene network, such as amorphous phase, non-six-membered rings or even heteroatoms. The graphitic degree, determined by the relative intensity of G band and D band (I_G/I_D) decreases in order of HGMC > GMC > Vulcan XC-72, as listed in Tab. 1, providing evidence for the higher graphitic degree of HGMC than GMC and Vulcan XC-72. Furthermore, the intensity of the peaks at 1200 cm^{-1} and 1510 cm^{-1}, related to amorphous phases, decreases significantly for HGMC and GMC comparing with Vulcan XC-72. Especially for HGMC, no observable resonance from amorphous phase can be distinguished in the spectrum. The Raman spectra results are completely consistent with that provided by the XRD analysis.

Tab. 1 Parameters for crystal structure of HGMC, GMC and Vulcan XC-72 analyzed from XRD patterns and Raman spectra

Sample	$2\theta_{(002)}$/(°)	$d_{(002)}$/nm	I_G/I_D
HGMC	26.2	0.34	0.98
GMC	26.2	0.34	0.61
Vulcan XC-72	24.8	0.36	0.52

The TEM images of the HGMC as well as MSGC are presented in Fig. 2A-2C. It can be seen that the HGMC is mainly composed of hollow spheres with a size of around 40 ~ 60 nm and piled nano ribbons. The graphitic shells of the hollow spheres are around 15 nm in thickness. In addition to the hollow spheres, a few of graphitic carbon enveloping large iron particles can also be observed. Such morphology is similar to that of the GMC reported in our previous work[25]. The formation of hollow structure can be explained by the silica particles and iron catalyst enveloped by the graphitic layers leaching out once treated in acid, while those en veloped fully by

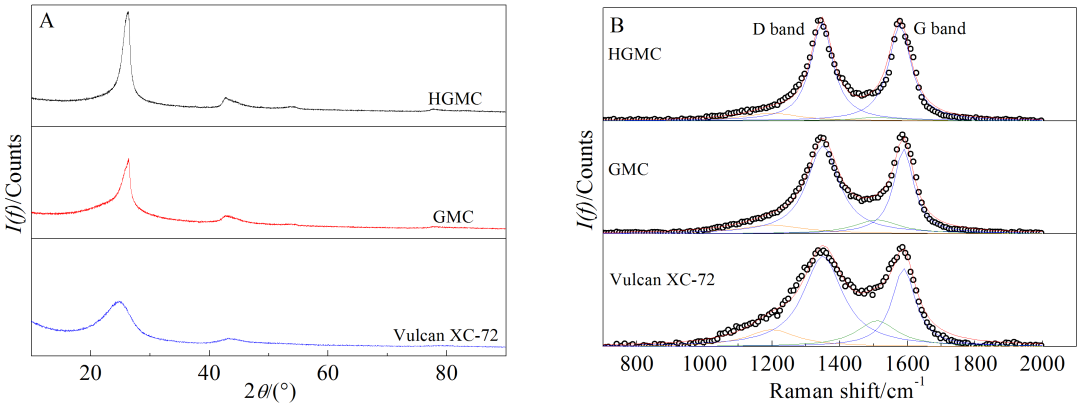

Fig. 1 XRD patterns (A) and Raman spectra (B) of HGMC, GMC and Vulcan XC-72

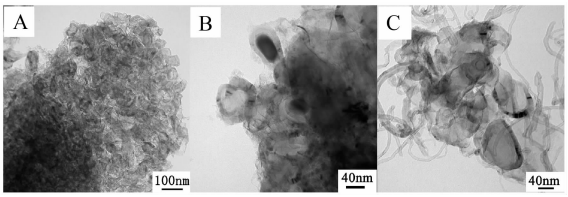

Fig. 2 TEM images of HGMC (A, B) and MSGC (C)

graphitic layers left.

The N_2 adsorption/desorption isotherms of the MSGC, HGMC, GMC and Vulcan XC-72 are shown in Fig. 3A. All of the samples exhibit type VI curves, indicating a micro-mesoporous structure. A typical difference between HGMC/GMC and Vulcan XC-72 is the appearance of hysteresis at higher P/P_0. As for HGMC/GMC, both of the hysteresis loops are type H3 which suggest that both HGMC and GMC have irregular mesopores, including slit, cylinder pores and so on. The Vulcan XC-72 has a H4 type hysteresis loop, suggesting that the Vulcan XC-72 has narrow slits on carbon sphere. As for MSGC, the N_2 adsorption/desorption isotherm resembles type VI, similar to that of HGMC. The surface areas of MSGC, HGMC, GMC and Vulcan XC-72 were obtained through multi-points BET method, in which the surface area contributed by micropores was calculated by the V-t plot method further and the results are listed in Tab. 2. It can be determined that the HGMC mainly contains mesopores while the GMC and Vulcan XC-72 have micropores. The pore size distributions of the four micro-mesoporous carbon samples were calculated by the DFT method other than BJH method applied previously since BJH method is appropr iate only for simulation of regular mesopores size. According to the types of N_2 adsorption/desorption isotherms, a calculation model of N_2 at 77 K on carbon (slit/cylinder pores, QSDFT adsorption branch) was chosen. From the pore size distribution shown in Fig. 3B, both micropores and mesopores contribute to the high surface area of the GMC, and the mesopores are mainly 3 ~ 4 nm in diameter, which is consistent with previous work. The micropores sized 1 ~ 2 nm in GMC samples, which were not considered in previous work, are possibly the slit generated in the imperfect laminar structure. Vulcan XC-72 possesses mediate surface area, 215.4 $m^2 \cdot g^{-1}$, yet with contribution from micropores up to 36.9% to the total area, both are less than as-received sample[25], which are 245 $m^2 \cdot g^{-1}$ and 54%, respectively. Although the HGMC possesses the lowest total specific surface area, 187.4 $m^2 \cdot g^{-1}$, it contains mainly mesopores (> 4 nm) partially generated from leaching out of silica and iron particles and the gas formed during the urea pyrolysis. As the physical mixture of HGMC and MWCNTs, MSGC inherits the characteristics of both HGMC and MWCNTs, i.e., mainly mesopores and compromise surface area 238.7 $m^2 \cdot g^{-1}$ due to the relatively higher specific surface area of MWCNTs, 286.7 $m^2 \cdot g^{-1}$.

The electrochemical stabilities of HGMC, GMC and Vulcan XC-72 are evaluated by mimicking the start-up/shut-down conditions of fuel cells in a three-electrode system. The test protocol is referred to the NREL standard[37-38], the electrode was scanned from 1.0 to 1.6 V with a sweeping rate of 100 $mV \cdot s^{-1}$ under room temperature. As shown in Fig. 4, for all

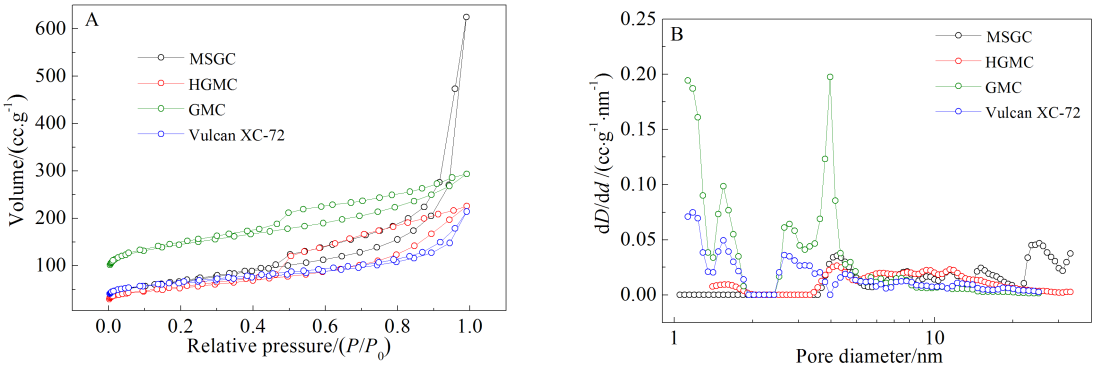

Fig. 3 N_2 adsorption-desorption isotherms (A) and pore size distribution curves (B) of MSGC, HGMC, GMC and Vulcan XC-72

Tab. 2 Surface areas of MSGC, HGMC, GMC and Vulcan XC-72 obtained from the N_2 adsorption/desorption isotherms

Sample	S_{BET}/ ($m^2 \cdot g^{-1}$)[1]	$S_{Micropore}$/ ($m^2 \cdot g^{-1}$)[2]	$S_{External}$/ ($m^2 \cdot g^{-1}$)[3]
MSGC	238.7	0	238.7
HGMC	187.4	0	187.4
GMC	522.6	279.3	243.3
Vulcan XC-72	215.4	79.5	135.9

[1] S_{BET} was calculated by multi-point BET method.
[2]-[3] $S_{Micropore}$ and $S_{External}$ were obtained by V-t plot method.

the three samples, the electrical double-layer capacitance is attributed to reversible charging/discharging of electrode-electrolyte interface and the redox peaks at 0.5 V are attributed to the reversible conversion between quinone and hydroquinone[39]. Initially, the electrical double-layers for HGMC and GMC are much thicker than that of Vulcan XC-72, indicating that the electrode-electrolyte interface areas for HGMC and GMC are larger. This is attributed to not only the high surface areas, but also high hydrophilicities of HGMC and GMC, while the high hydrophilicities of HGMC and GMC are ascribed to the high oxygen contents of carbon precursor. Compared to GMC, the electrical double-layer current for HGMC is lower, which is associated with the lower surface area of HGMC than that of GMC. After the accelerating aging test, the double-layer thickness for the HGMC is almost unchanged, while 23% increase of the initial for GMC and up to 300% increase of that for Vulcan XC-72 can be observed. The final double-layer capacitance of the three samples decreases in order of GMC > Vulcan XC-72 > HGMC, completely consistent to that of BET surface area. From the above analysis, both Vulcan XC-72 and GMC suffer from electrochemical corrosion during AAT, which leading to the increase of surface groups, and moreover, higher surface hydrophilicity[40]. The HGMC is much more stable as expected benefiting from the higher graphitic degree of carbon and lower content

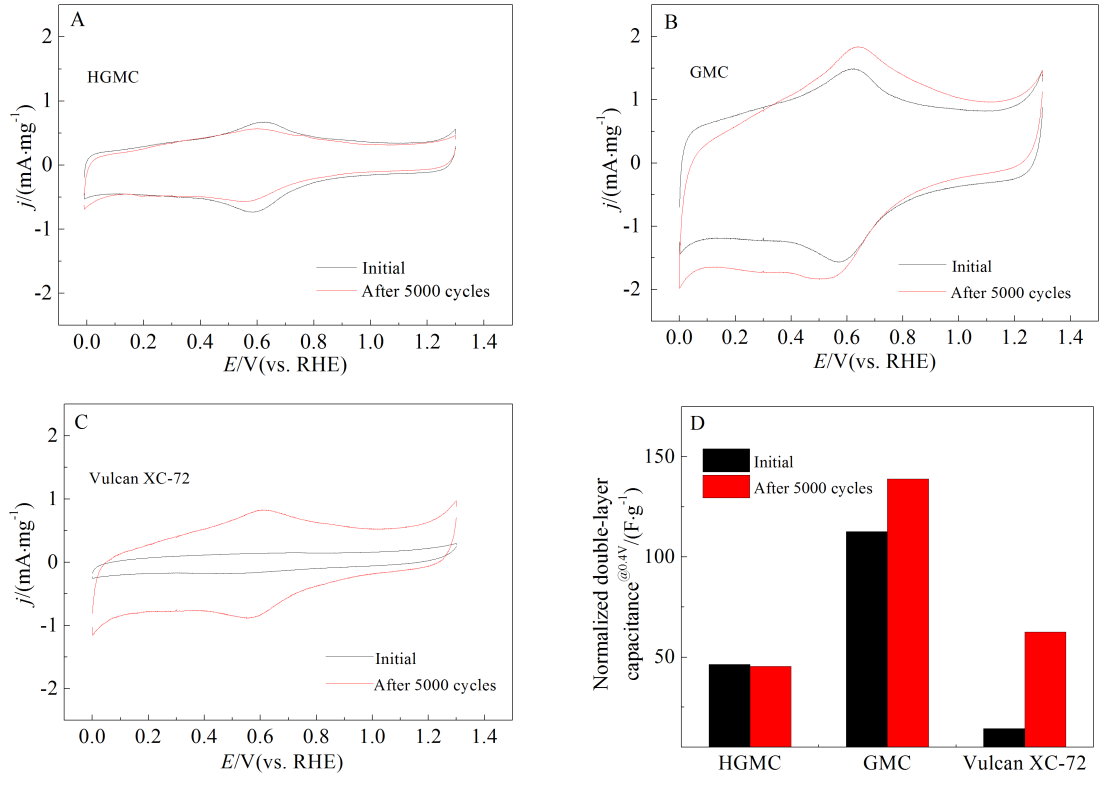

Fig. 4 Cyclic voltammograms of HGMC (A), GMC (B) and Vulcan XC-72 (C) in N_2-purged 0.1 mol·L^{-1} $HClO_4$ with a scan rate of 10 mV·s^{-1}. The variations of electrical double-layer capacitance before and after the AAT (D)

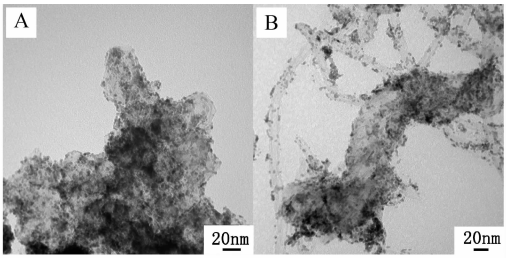

Fig. 5 TEM images of Pt/HGMC (A) and Pt/MSGC (B)

of defects as well as amorphous phase.

The TEM images of Pt/HGMC and Pt/MSGC are shown in Fig. 5. For both electrocatalysts, the Pt nanoparticles are populated but highly dispersed on carbon supports with the average particle size of around 3 nm (Fig. 9B), which is smaller than that of the Pt/C-JM (~ 4 nm, Fig. 9B). The smaller Pt particle of the home-made samples justifies the effectivity of the polyol synthesis approach. For the multi-scaled supports in Fig. 5B, the density of Pt particles on the MWCNTs is a little less than on the HGMC, probably due to fewer anchoring sites on the former. Thus, the major role of the MWCNTs is expected to be a spacer to facilitate the mass transport of reactants, which will be discussed below based on the electrochemical performance.

The background cyclic voltammograms and the ORR polarization curves of Pt/HGMC and Pt/ MSGC, together with the Pt/C-JM, are plotted in Fig. 6. Electrochemical surface areas (ECSAs) were obtained by calculating the charge of the underpotential desorption of atomic hydrogen (H_{upd}) between 0.05 to 0.42 V in the background cyclic voltammograms assuming a constant of 0.21 mC·cm$^{-2}_{Pt}$. To compare clearly, the ECSAs, the half-wave potentials ($E_{1/2}$) and the ORR mass activities (@0.9 V) of the three catalysts are listed in Table 3. The ECSA values of Pt/HGMC, Pt/MSGC and Pt/C-JM are 28.5, 50.2 and 37.2 m^2·g^{-1} respectively. The much lower ECSAs of the Pt/HGMC as compared to those of Pt/MSGC and Pt/C-JM suggests the low utilization of Pt in Pt/HGMC most likely due to the laminar structure of HGMC since the Pt particle sizes for Pt/HGMC and Pt/MSGC are similar. Accordingly, the $E_{1/2}$ of the ORR over the Pt/HGMC is more negative than that over the Pt/C-JM. After introducing MWCNTs as the spacer, the utilization of Pt is increased significantly reflected by the higher ECSA for the Pt/MSGC, indicating that the transportation of the electrolyte and the reactant is enhanced in the 3D multi-scaled supports. The higher ECSA of the Pt/MSGC as compared to the Pt/C-JM is due to the smaller Pt particles on MSGC as shown in Fig 8. In summary, both higher dispersion of Pt particles and enhanced transportation of the electrolyte and the reactant contribute to the high ORR activity of Pt/MSGC.

The stability of the Pt/MSGC was tested by running the AAT protocol. The background CVs, ORR polarization curves and the derived ECSAs and the mass activities of the two catalysts before and after the AAT are plotted in Fig. 7. After 10000 cycles, the

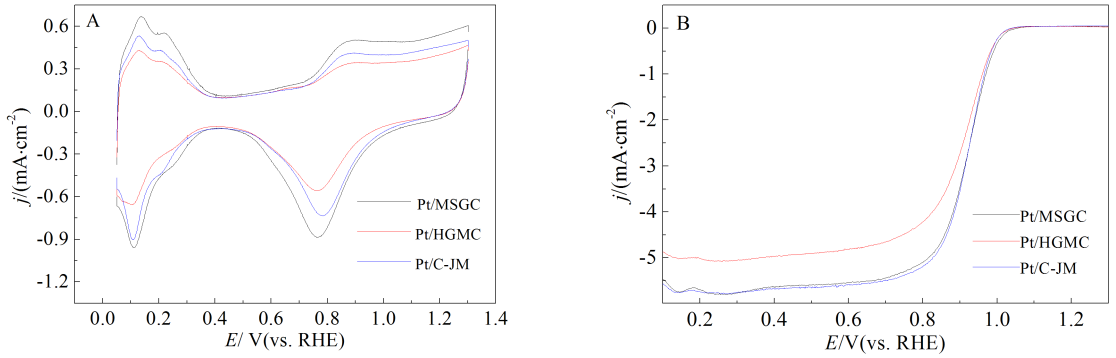

Fig. 6 Cyclic voltammograms (CVs) (A) and ORR polarization curves (B) of Pt/HGMC, Pt/MSGC and Pt/C-JM. The background CVs were obtained in N_2-purged 0.1 mol·L^{-1} $HClO_4$ with a scan rate of 10 mV·s^{-1} and the ORR polarization curves were obtained under the same scan rate with a rotating speed of 1600 r·min^{-1}. The Pt loading was 0.1 mg·cm^{-2}.

Tab. 3 The ECSA, $E_{1/2}$ and mass activity values of Pt/HGMC, Pt/MSGC and Pt/C-JM

Sample	ECSA/ ($m^2 \cdot g^{-1}_{Pt}$)	$E_{1/2}$/ mV(vs. RHE)	MA/ ($mA \cdot mg^{-1}_{Pt}$)
Pt/HGMC	28.5	896	59.3
Pt/MSGC	50.2	917	87.5
Pt/C-JM	37.2	917	83.8

electrical double-layer current of the Pt/C-JM increased slightly due to the electrochemical oxidation of carbon support. It should be noted that the limiting current of the ORR over the Pt/C-JM in Fig. 7D is apparently decreased as compared to that over the Pt/MSGC, which is deduced that some Pt particles may detach from the carbon support due to the corrosion of carbon. The ECSA decreased by 39% of the initial (from 37.2 to 22.9 $m^2 \cdot g^{-1}_{pt}$) for the Pt/C-JM and 21% (from 50.2 to 39.7 $m^2 \cdot g^{-1}_{pt}$) for the Pt/MSGC. Loss of ECSA brings up degradation of the ORR activity. After the ATT, the $E_{1/2}$ values of the ORR over the Pt/MSGC and Pt/C-JM shift negatively about 11 mV, respectively, and the kinetically mass-normalized ORR current (@0.9 V) over the Pt/MSGC de-

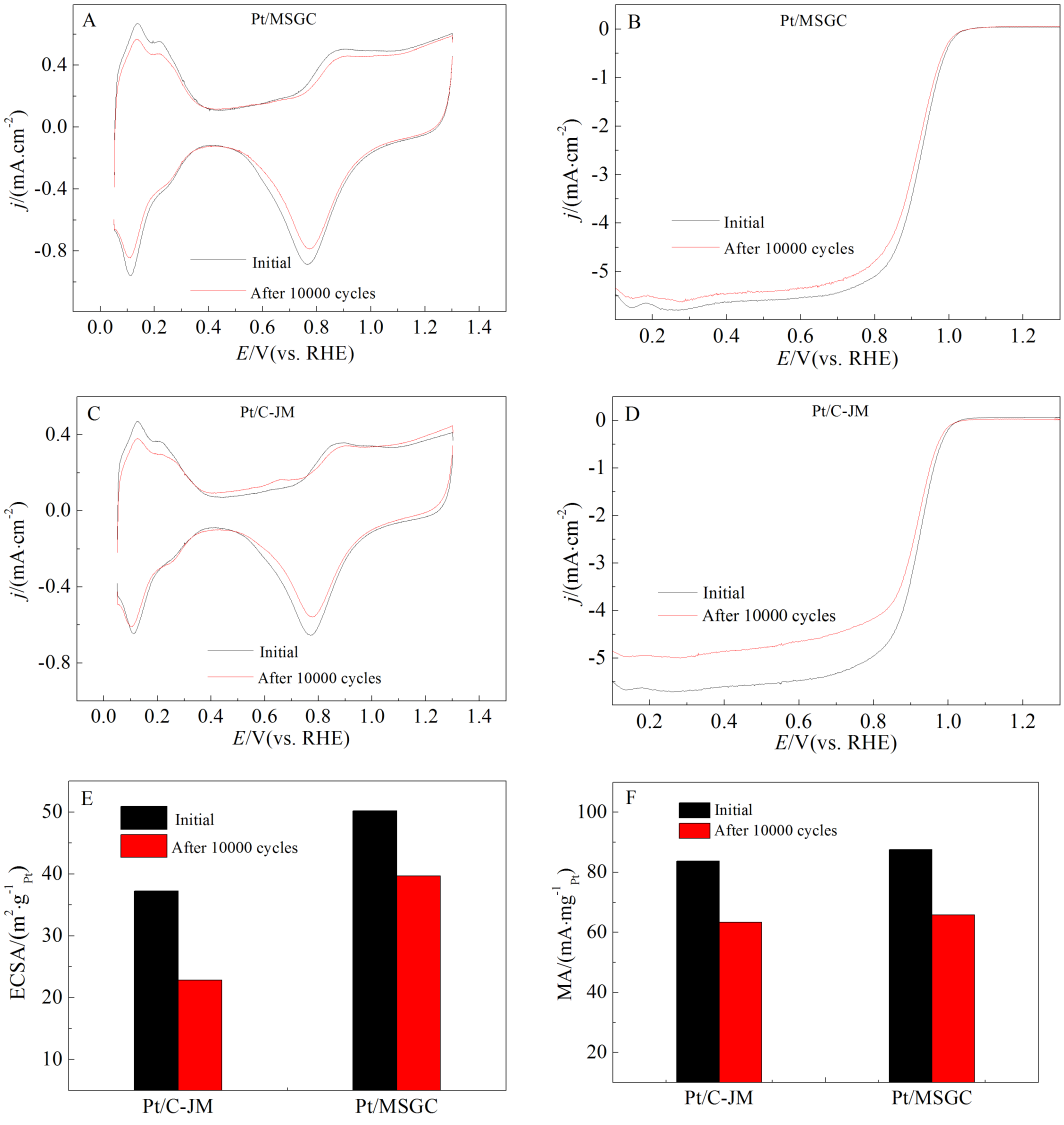

Fig. 7 CVs and ORR polarization curves of Pt/MSGC (A, B) and Pt/ C-JM (C, D) with a scan rate of 10 $mV \cdot s^{-1}$ in 0.1 $mol \cdot L^{-1}$ $HClO_4$. ECSAs (E) and the Pt mass normalized kinetic current density at 0.9 V (vs. RHE) (F) before and after accelerating aging test. The Pt loading was 0.1 $mg \cdot cm^{-2}$.

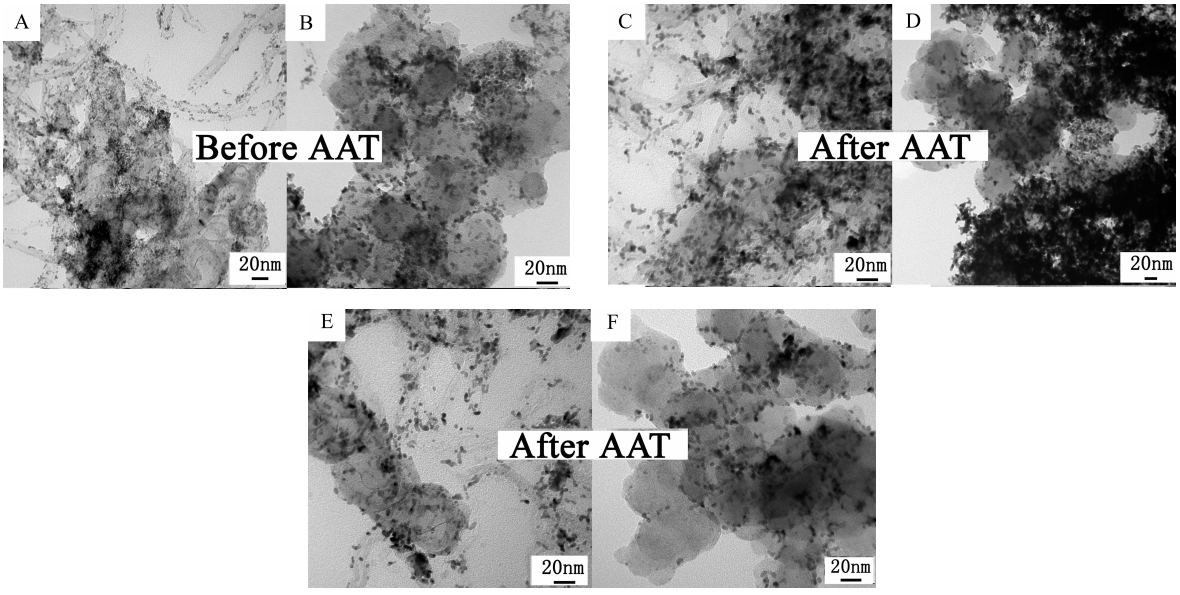

Fig. 8 TEM images of Pt/MSGC (A, C, E) and Pt/C-JM (B, D, F) before and after the accelerating aging test

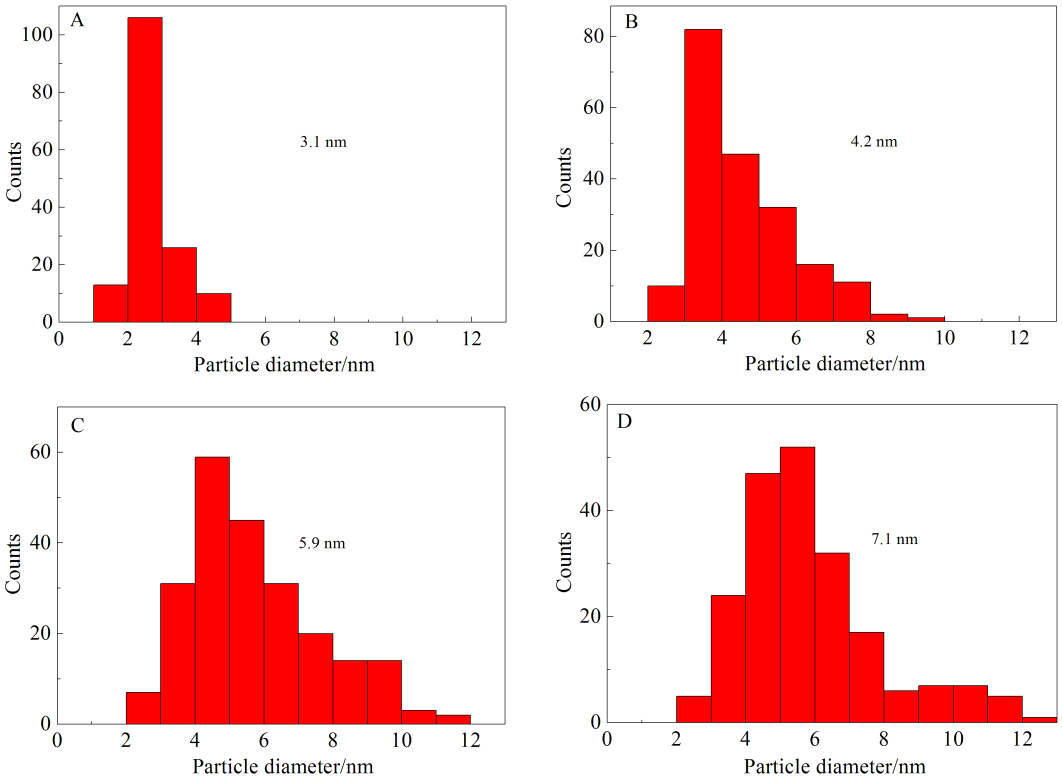

Fig. 9 The Pt particle size distributions and the mean particle sizes in Pt/MSGC (A, C) and Pt/C-JM (B, D) before and after the accelerating aging test statistically from the TEM images in Fig. 8A-D

creases by 24.8% (from 87.5 to 65.8 mA·mg$^{-1}_{Pt}$), similar to that of the Pt/C-JM (24.4%, from 83.8 to 63.3 mA·mg$^{-1}_{Pt}$). It is interesting that, although the ECSA of the Pt/C-JM decreased more seriously than that of the Pt/MSGC, the ORR degradation degrees for both catalysts are similar. Considering that the Pt loading on the glassy carbon is as high as 0.1 mg·cm^{-2}, such a decreased degree in the ECSA may not influence sig-

nificantly on the ORR performance.

To clarify the causes responsible for the ECSA loss, and therefore, the ORR performance degradation, the morphologies of the Pt/MSGC and Pt/C-JM before and after the AAT were characterized by TEM. It can be identified that, after 10000 potential cycling, the Pt nanoparticles for the Pt/MSGC (Fig. 8C, 8E) aggregated slightly with the average particle size increasing from 3.1 nm to 5.9 nm (Fig. 9A, 9C). In contrast, the Pt nanoparticles for the Pt/C-JM (Fig. 8D) aggregated seriously from 4.2 nm to 7.1 nm (Fig. 9B, 9D). Additionally, we observed the Pt density is sparse in some regions for the Pt/C-JM, as shown in Fig. 8F, which leads to the irregular dispersion of platinum on working electrode and even further, the significant decrease of limiting current. Both the aggregation and the sparse density of Pt particles for the Pt/C-JM suggest that the carbon support was corroded. In contrast, MSGC is much more stable than Vulcan XC-72 under the same severe condition.

3 Conclusions

The HGMC was synthesized by using resorcinol resin as the carbon precursor and SiO_2 as the templates. The obtained HGMC is of a moderate surface area (187.4 $m^2 \cdot g^{-1}$) and is chemically stable under potentiodynamic cycling as compared to the commercial Vulcan XC-72, while the high graphitic structure is adverse to the mass transport. To overcome the drawback of the HGMC in mass transportation, MWCNTs was introduced as a spacer to construct a 3D multi-scaled support. Compared to the single HGMC supported Pt catalyst and the commercial Pt/C-JM catalyst, the multi-scaled MSGC supported Pt catalyst displayed both enhanced electrochemical stability and significantly improved mass transportation for the ORR, due to the stability and the multi-scaled structure of the carbon supports.

References:

[1] Wilson M S, Gottesfeld S. High performance catalyzed membranes of ultra-low pt loadings for polymer electrolyte fuel cells [J]. Journal of The Electrochemical Society, 1992, 139(2): L28-L30.

[2] Wilson M S, Gottesfeld S. Thin-film catalyst layers for polymer electrolyte fuel cell electrodes [J]. Journal of Applied Electrochemistry, 1992, 22(1): 1-7.

[3] Reiser C A, Bregoli L, Patterson T W, et al. A reverse-current decay mechanism for fuel cells[J]. Electrochemical and Solid-State Letters, 2005, 8(6): A273-A276.

[4] Stevens D A, Hicks M T, Haugen G M, et al., Ex situ and in situ stability studies of PEMFC catalysts: Effect of carbon type and humidification on degradation of the carbon [J]. Journal of The Electrochemical Society, 2005, 152 (12): A2309-A2315.

[5] Schlögl K, Hanzlik M, Arenz M, Comparative IL-TEM study concerning the degradation of carbon supported pt-based electrocatalysts[J]. Journal of The Electrochemical Society, 2012, 159(6): B677-B682.

[6] Roen L M, Paik C H, Jarvi T D, Electrocatalytic corrosion of carbon support in PEMFC cathodes[J]. Electrochemical and Solid-State Letters, 2004, 7(1): A19-A22.

[7] Meier J C, Galeano C, Katsounaros I, et al., Degradation mechanisms of Pt/C fuel cell catalysts under simulated start-stop conditions[J]. ACS Catalysis, 2012, 2(5): 832-843.

[8] Mayrhofer K J J, Ashton S J, Meier J C, et al. Non-destructive transmission electron microscopy study of catalyst degradation under electrochemical treatment[J]. Journal of Power Sources, 2008, 185(2): 734-739.

[9] Rabis A, Rodriguez P, Schmidt T J. Electrocatalysis for polymer electrolyte fuel cells: Recent achievements and future challenges[J]. ACS Catalysis, 2012, 2(5): 864-890.

[10] Schulenburg H, Schwanitz B, Linse N, et al. 3D imaging of catalyst support corrosion in polymer electrolyte fuel cells[J]. The Journal of Physical Chemistry C, 2011, 115 (29): 14236-14243.

[11] Shao Y, Yin G, Gao Y, et al. Durability study of Pt/C and Pt/CNTs catalysts under simulated PEM fuel cell condi tions[J]. Journal of The Electrochemical Society, 2006, 153(6): A1093-A1097.

[12] Okamoto M, Fujigaya T, Nakashima N. Design of an assembly of poly(benzimidazole), carbon nanotubes, and Pt nanoparticles for a fuel-cell electrocatalyst with an ideal interfacial nanostructure[J]. Small, 2009, 5(6): 735-740.

[13] Maiyalagan T, Viswanathan B, Varadaraju U V. Nitrogen containing carbon nanotubes as supports for Pt - alternate anodes for fuel cell applications[J]. Electrochemistry Communications, 2005, 7(9): 905-912.

[14] Hasche F, Oezaslan M, Strasser P. Activity, stability and degradation of multi walled carbon nanotube (MWCNT) supported Pt fuel cell electrocatalysts[J]. Physical Chemistry Chemical Physics, 2010, 12(46): 15251-15258.

[15] Hafez I H, Berber M R, Fujigaya T, et al. Enhancement

of platinum mass activity on the surface of Polymer-wrapped carbon nanotube-based fuel cell electrocatalysts[J]. Scientific Reports, 2014, 4: 6295.

[16] Fujigaya T, Okamoto M, Nakashima N. Design of an assembly of pyridine-containing polybenzimidazole, carbon nanotubes and Pt nanoparticles for a fuel cell electrocatalyst with a high electrochemically active surface area[J]. Carbon, 2009, 47(14): 3227-3232.

[17] Fujigaya T, Nakashima N. Fuel cell electrocatalyst using polybenzimidazole-modified carbon nanotubes as support materials[J]. Advanced Materials, 2013, 25(12): 1666-1681.

[18] Fujigaya T, Hirata S, Nakashima N. A highly durable fuel cell electrocatalyst based on polybenzimidazole-coated stacked graphene[J]. Journal of Materials Chemistry A, 2014, 2(11): 3888-3893.

[19] Du H Y, Wang C H, Yang C S, et al. A high performance polybenzimidazole-CNT hybrid electrode for high-temperature proton exchange membrane fuel cells[J]. Journal of Materials Chemistry A, 2014, 2(19): 7015-7019.

[20] Zhang L W, Zheng N, Gao A, et al. A robust fuel cell cathode catalyst assembled with nitrogen-doped carbon nanohorn and platinum nanoclusters[J]. Journal of Power Sources, 2012, 220: 449-454.

[21] Yoshitake T, Shimakawa Y, Kuroshima S, et al. Preparation of fine platinum catalyst supported on single-wall carbon nanohorns for fuel cell application[J]. Physica B: Condensed Matter, 2002, 323(1/4): 124-126.

[22] Kou R, Shao Y Y, Wang D H, et al. Enhanced activity and stability of Pt catalysts on functionalized graphene sheets for electrocatalytic oxygen reduction[J]. Electrochemistry Communications, 2009, 11(5): 954-957.

[23] Maruyama J, Sumino K-i, Kawaguchi M, et al. Influence of activated carbon pore structure on oxygen reduction at catalyst layers supported on rotating disk electrodes[J]. Carbon, 2004, 42(15): 3115-3121.

[24] Maruyama J, Abe I. Effective utilization of nanospaces in activated carbon for enhancing catalytic activity in fuel cell electrodes[J]. Journal of The Electrochemical Society, 2004, 151(3): A447-A451.

[25] Qi J, Jiang L H, Wang S L, et al. Synthesis of graphitic mesoporous carbons with high surface areas and their applications in direct methanol fuel cells[J]. Applied Catalysis B: Environmental, 2011, 107(1/2): 95-103.

[26] Zhou Z H, Wang S L, Zhou W L, et al. Novel synthesis of highly active Pt/C cathode electrocatalyst for direct methanol fuel cell[J]. Chemical Communications, 2003, 3: 394-395.

[27] Gloaguen F, Andolfatto F, Durand R, et al. Kinetic study of electrochemical reactions at catalyst-recast ionomer interfaces from thin active layer modelling[J]. Journal of Applied Electrochemistry, 1994, 24(9): 863-869.

[28] Paulus U A, Schmidt T J, Gasteiger H A, et al. Oxygen reduction on a high-surface area Pt/Vulcan carbon catalyst: a thin-film rotating ring-disk electrode study[J]. Journal of Electroanalytical Chemistry, 2001, 495 (2): 134-145.

[29] Garsany Y, Baturina O A, Swider-Lyons K E, et al. Experimental methods for quantifying the activity of platinum electrocatalysts for the oxygen reduction reaction [J]. Analytical Chemistry, 2010, 82(15): 6321-6328.

[30] Õya A, Marsh H. Phenomena of catalytic graphitization [J]. Journal of Materials Science, 1982, 17(2): 309-322.

[31] Marsh H, Crawford D, Taylor D W. Catalytic graphitization by iron of isotropic carbon from polyfurfuryl alcohol, 725-1090 K. A high resolution electron microscope study [J]. Carbon, 1983, 21(1): 81-87.

[32] Derbyshire F J, Presland A E B, Trimm D L. Graphite formation by the dissolution-precipitation of carbon in cobalt, nickel and iron[J]. Carbon, 1975, 13(2): 111-113.

[33] Lei Z, Lu L, Zhao X S. The electrocapacitive properties of graphene oxide reduced by urea[J]. Energy & Environmental Science, 2012, 5(4): 6391-6399.

[34] Sevilla M, Sanchí s C, Valdé s-Solís T, et al. Synthesis of graphitic carbon nanostructures from sawdust and their application as electrocatalyst supports[J]. The Journal of Physical Chemistry C, 2007, 111(27): 9749-9756.

[35] Wu G, Mack N H, Gao W, et al. Nitrogen-doped graphene-rich catalysts derived from heteroatom polymers for oxygen reduction in nonaqueous Lithium-O_2 battery cathodes[J]. ACS Nano, 2012, 6(11): 9764-9776.

[36] Tuinstra F, Koenig J L. Raman spectrum of graphite[J]. The Journal of Chemical Physics, 1970, 53(3): 1126-1130.

[37] Mason K S, Neyerlin K C, Kuo M-C, et al. Investigation of a silicotungstic acid functionalized carbon on Pt activity and durability for the oxygen reduction reaction[J]. Journal of The Electrochemical Society, 2012, 159 (12): F871-F879.

[38] Riese A, Banham D, Ye S, et al. Accelerated stress testing by rotating disk electrode for carbon corrosion in fuel cell catalyst supports[J]. Journal of The Electrochemical Society, 2015, 162(7): F783-F788.

[39] Tarasevich M R, Bogdanovskaya V A, Zagudaeva N M. Redox reactions of quinones on carbon materials [J]. Journal of Electroanalytical Chemistry and Interfacial

Electrochemistry, 1987, 223(1/2): 161-169.
[40] Artyushkova K, Pylypenko S, Dowlapalli M, et al. Structure-to-property relationships in fuel cell catalyst supports: Correlation of surface chemistry and morphology with oxidation resistance of carbon blacks [J]. Journal of Power Sources, 2012, 214: 303-313.

多尺度炭材料担载铂作为稳定的电催化剂用于氧还原反应

李玉萍[1,2],姜鲁华[1*],王素力[1],孙公权[1*]
(1. 大连洁净能源国家重点实验室(筹), 中国科学院大连化学物理研究所, 辽宁 大连 116023;
2. 中国科学院大学, 北京 100039)

摘 要: 炭载体的稳定性对于燃料电池电催化剂是至关重要的. 本文中采用酚醛树脂作为前驱体,二氧化硅为模板剂,制备了多介孔且石墨化程度高的炭载体(HGMC). 相比于商品 Vulcan XC-72,HGMC 具有中等的比表面积和高的石墨化程度,因此在电位循环扫描过程中具有较高的化学稳定性,然而 HGMC 碳层堆叠的结构不利于传质. 为克服这一劣势,多壁碳纳米管(MWCNTs)作为隔离物加入至 HGMC 中以构建具有三维多尺度结构的载体(MSGC). 与 HGMC 为载体担载 Pt 以及商品催化剂 Pt/C-JM 相比, 由于炭载体的具有高稳定性以及三维多尺度结构,MSGC 担载 Pt 后不仅使电催化剂的电化学稳定性提高,且氧还原反应过程中传质得到显著改善.

关键词: 炭载体;铂;氧还原反应;燃料电池